Citation
Li, H. and Chen, W. and Huang, Z. and Hao, H. and Ngo, T.T. and Pham, T.M. 2022. Influence of various impact scenarios on the dynamic performance of concrete beam-column joints. International Journal of Impact Engineering. 167: ARTN 104284.
http://doi.org/10.1016/j.ijimpeng.2022.104284

Influence of various impact scenarios on the dynamic performance of concrete beam-column joints

Huawei Li[1,2], Wensu Chen[2]*, Zhijie Huang[2], Hong Hao[2]*, Tuan T. Ngo[2,3], Thong M. Pham[2]

[1]Guangzhou University-Curtin University Joint Research Center for Structural Monitoring and Protection against Multi-Dynamic Hazards, School of Civil Engineering, Guangzhou University, China

[2]Center for Infrastructural Monitoring and Protection, School of Civil and Mechanical Engineering, Curtin University, Australia

[3]Faculty of Engineering and Technology, Quy Nhon University, Viet Nam

* Corresponding authors: wensu.chen@curtin.edu.au (W. Chen), hong.hao@curtin.edu.au (H. Hao)

https://doi.org/10.1016/j.ijimpeng.2022.104284

Abstract: This study investigated dynamic performances of concrete beam-column joints under various impact loading scenarios including impact contact condition (i.e., impact directly or via an interlayer), impact location, and impact loading pattern (i.e., concentrated or distributed loads). The influence of impact contact conditions was experimentally studied by a pendulum impact testing system. The test results showed that the softer contact by using a rubber pad led to an impact force profile with a less prominent force peak but resulted in more flexural concrete cracks on the beam. Furthermore, the finite element models of beam-column joints under impact were developed and verified by the test results. Based on the calibrated numerical models, the effects of impact location and impact loading pattern on the dynamic performances of joints were investigated. It was found that the specimens exhibited more flexural-governed cracks as the impact location moved away from the joint area. In addition, the distributed impact loading pattern resulting from an impactor with a wider contact area caused higher impact force, larger displacement response of beam, and severer damage at joint area than those generated by the concentrated impact loading pattern of the same kinetic energy, indicating the distributed impact loading is a more dangerous impact scenario to the safety of beam-column joints.

Keywords: Impact scenario; Contact stiffness; Impact location; Impact loading pattern; Precast concrete; Beam-column joint

1. Introduction

Beam-column joints connecting beams and columns are important components to transfer loads and maintain the integrity of structures. Beam-column joints should be designed to have sufficient robustness to avoid the progressive collapse of structures under extreme loads such as impact and blast loads [1, 2]. With the recent development in reinforced concrete (RC) construction techniques, the use of precast concrete (PC) has become an increasingly important method due to several merits such as fast construction and cost-effectiveness. PC beam-column joints with wet connections are usually designed with emulative details to match the capacity of monolithic RC joints, which show the great application potential of PC joints [3-5].

Extensive studies on seismic performances of PC joints with wet connections have been conducted to improve their design and construction efficiency [6, 7]. Some experimental studies have been carried out to investigate the seismic performance of PC joints under cyclic loading [8-13]. It is found that the PC joints have comparable or superior performance than the monolithic RC joints if appropriate construction details of joints are designed. However, failure modes of PC joints are different from those of monolithic RC joints. Cracks initiate and spread intensively at the interface between the PC and cast-in-place (CIPC) components in the PC joints, while cracks are more evenly distributed in the plastic zone and the core area of beam-column joint in the conventional monolithic RC joints. The roughened interface and additional reinforcement passing through the interface can be employed to improve the bonding of interfaces in PC joints against cyclic loadings [13, 14]. Besides, the static behaviors of PC beam-column joints with wet connections to resist progressive collapse were experimentally investigated by quasi-static pushdown loadings [15-18]. Concrete cracks are prone to appear along the wet interface during the loading process, which again confirms that the wet connection is the weak part of the PC joint.

In addition to seismic loading and quasi-static pushdown loading, the beam-column joint may suffer impact loading from various sources such as falling components [19, 20] as illustrated in Fig. 1. The failed structural members of the upper floor during extreme events could cause the falling of structural and non-structural members. The falling components impact the lower floor and thus could cause damage to joints at the lower floor. The structure might collapse subsequently if the joints cannot resist the impact loads. Therefore, it is essential to examine the dynamic behavior of beam-column joints under the falling component impact.

To date, there are many experimental and numerical studies on the impact behavior of concrete beams [21, 22], columns [23, 24], and slabs [25, 26]. However, investigations on the impact behavior of concrete beam-column joints, especially PC beam-column joints are still limited. Li et al. [27] experimentally and numerically studied the influence of wet connection configurations on the dynamic responses of beam-column joints under impact loads. The PC beam-column joints with shear keys or interface rebars are more effective to resist shear-governed response induced by impact loading. Ngo et al. [28] carried out pendulum impact tests on PC beam-column dry joints with GFRP bolts, GFRP reinforcements, and various types of fiber reinforcements in concrete. The existence of fiber could reduce the damage level and displacement response of joints. These two studies mainly focus on the effects of beam-column joint types and construction methods on their impact-resistant performance.

Besides, it is worth noting that the randomness of falling components generates various impact scenarios such as different contact conditions at the impact zone, different impact locations, and different loading patterns. In the falling impact events as illustrated in Fig. 1(a), the falling members might impact the lower floor directly or impact onto the existing falling debris that has located at the impact zone, which results in different contact stiffness between impactor and structure. It has been reported in the previous study of beams under impact loading that different contact conditions could cause different impact force profiles and amplitudes [29]. Moreover, the impact location could be close to or away from the joint area as shown in Fig. 1(b). The impact loading induced by the falling component might be either concentrated or distributed in an area due to the shapes of falling components as shown in Fig. 1(b) and Fig.

1(c), respectively. These different impact scenarios certainly incur different dynamic responses of beam-column joints. However, there is no systematic study of the dynamic performances of beam-column joint under different impact scenarios in the open literature yet. Therefore, understanding the dynamic response of a joint under various falling impact scenarios is critical for the effective designs of joints to resist such hazards.

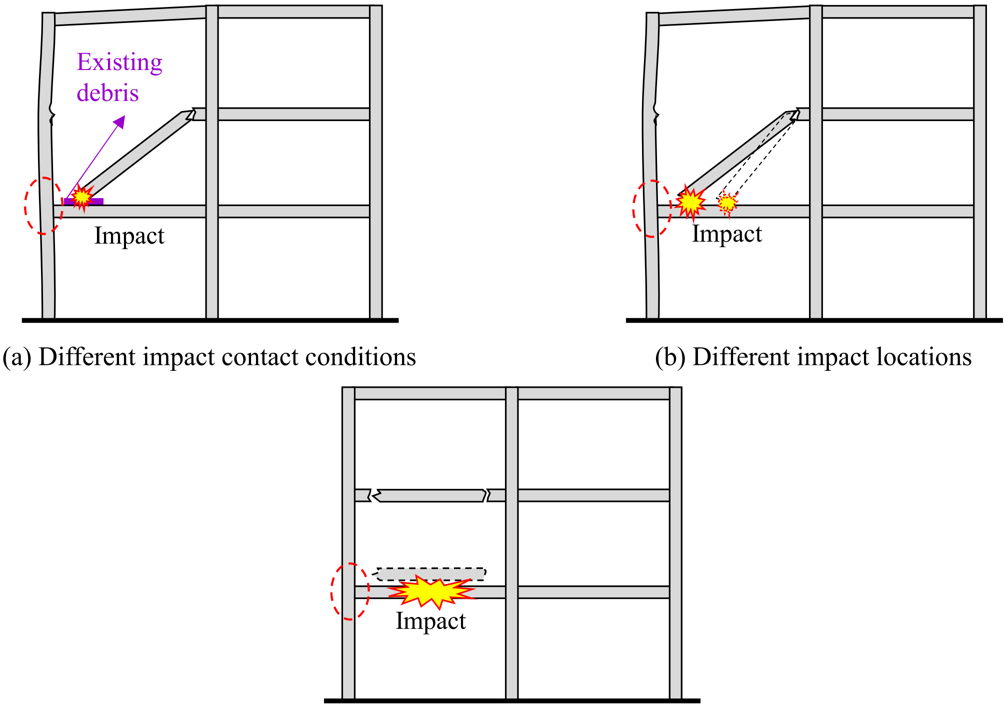

(a) Different impact contact conditions

(b) Different impact locations

(c) Different impact loading patterns

Fig. 1. Different impact scenarios.

This study carried out experimental and numerical investigations to gain insights into the impact behavior of beam-column joints subjected to various impact scenarios. The influence of contact condition (i.e., with or without rubber pad) on the impact behavior of joint was experimentally investigated. Moreover, detailed finite element models of the PC beam-column joints were established using LS-DYNA and verified against the testing data. Then the verified numerical models were employed to assess the influences of impact location and impact loading pattern on the impact behavior of concrete beam-column joints.

2. Experimental program

2.1. Specimen preparation

A monolithic RC joint (MCJ-RP) and a PC joint (PCJ-RP) were designed and prepared in this study as shown in Fig. 2. The emulative detailing was employed for the PC joint to achieve an equivalent performance of the monolithic RC joint. These joint specimens had the same geometric dimension and rebar layout. The width, depth, and length of beams were 200 mm, 150 mm, and 800 mm, respectively as presented in Fig. 2. The column was 200 mm square and its total length was 1280 mm. Four longitudinal rebars were arranged in the beam sections. The diameters of steel longitudinal rebars and stirrups employed in beams were 16 mm and 10 mm, respectively. The longitudinal rebars in beams extended into the joint area with 90° hooked anchorage to increase the joint integrity and bond strength. The column section was reinforced by four longitudinal rebars with a diameter of 16 mm. The stirrup spacing at the joint and other area was respectively 50 mm and 70 mm as shown in Fig. 2. The construction procedures to assemble the beam-column joints were similar to those introduced by the authors in the previous study [27]. The concrete compressive strength for PC and CIPC components were 64.75 MPa and 68.34 MPa, respectively. The yield strength and ultimate strength of longitudinal rebars were 539 MPa and 696 MPa, and those of stirrups were 523 MPa and 692 MPa, respectively.

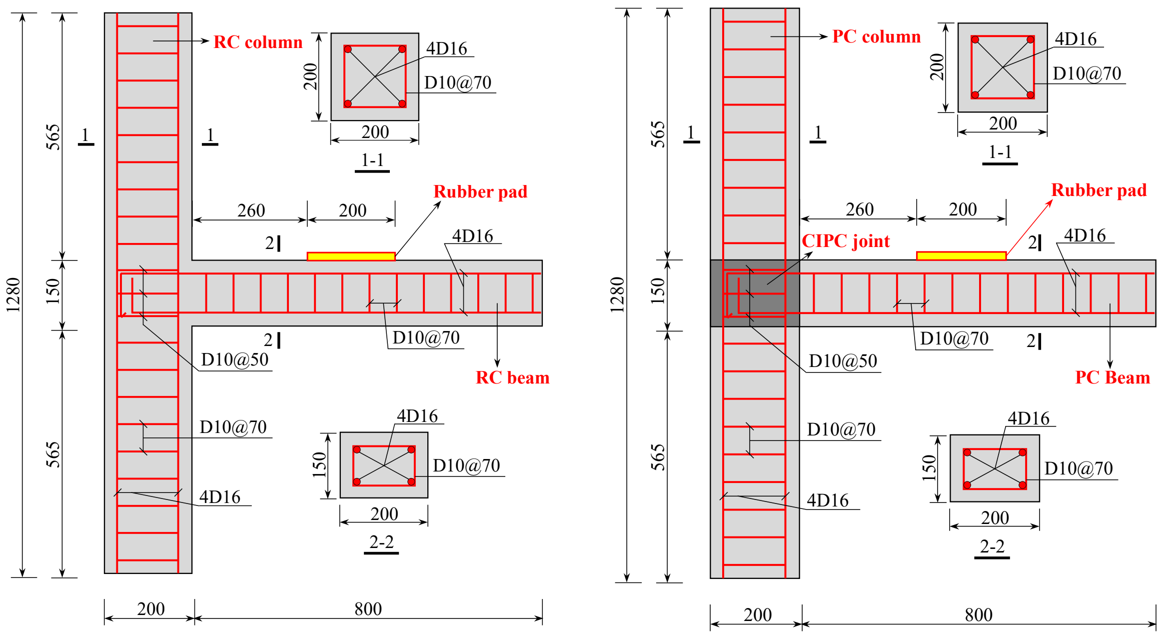

(a) MCJ-RP (b) PCJ-RP

Fig. 2. Design of tested joint specimens.

2.2. Impact test setup

A pendulum impact testing system was employed to conduct the impact test of beam-column joint specimens as shown in Fig. 3. The impact loading was applied on the beam by an impactor with a mass of 550 kg to simulate the falling impact scenarios as shown in Fig. 1. The impactor was released from a designated angle θ and then impacted the beam (i.e., at the center of rubber pad in this study). The impactor was pulled back immediately by a winch after the impact to avoid subsequent impact on the beam. The impact force acting on the specimen was measured by a load cell installed in front of the impact mass. The joint specimens were hinge-supported at the column ends with a center distance of 1030 mm. The reaction forces acting on the column during impact were measured by load cells placed at the bottom of the vertical supports. Signals of the impact and reaction forces were recorded at a sampling rate of 50 kHz. An axial force of 60 kN was applied on the column top by a hydraulic jack at the right side of the test setup as shown in Fig. 3. The applied axial force was small (about 2% of the axial load-carrying capacity of column) to minimize its beneficial effects on the capacity of the joints and to avoid initial damage to the specimen. The impact processes of the joint specimens were captured by a high-speed camera with a sampling rate of 20,000 frames per second. The tracking point shown in Fig. 3 was employed to measure the displacement at the impact location.

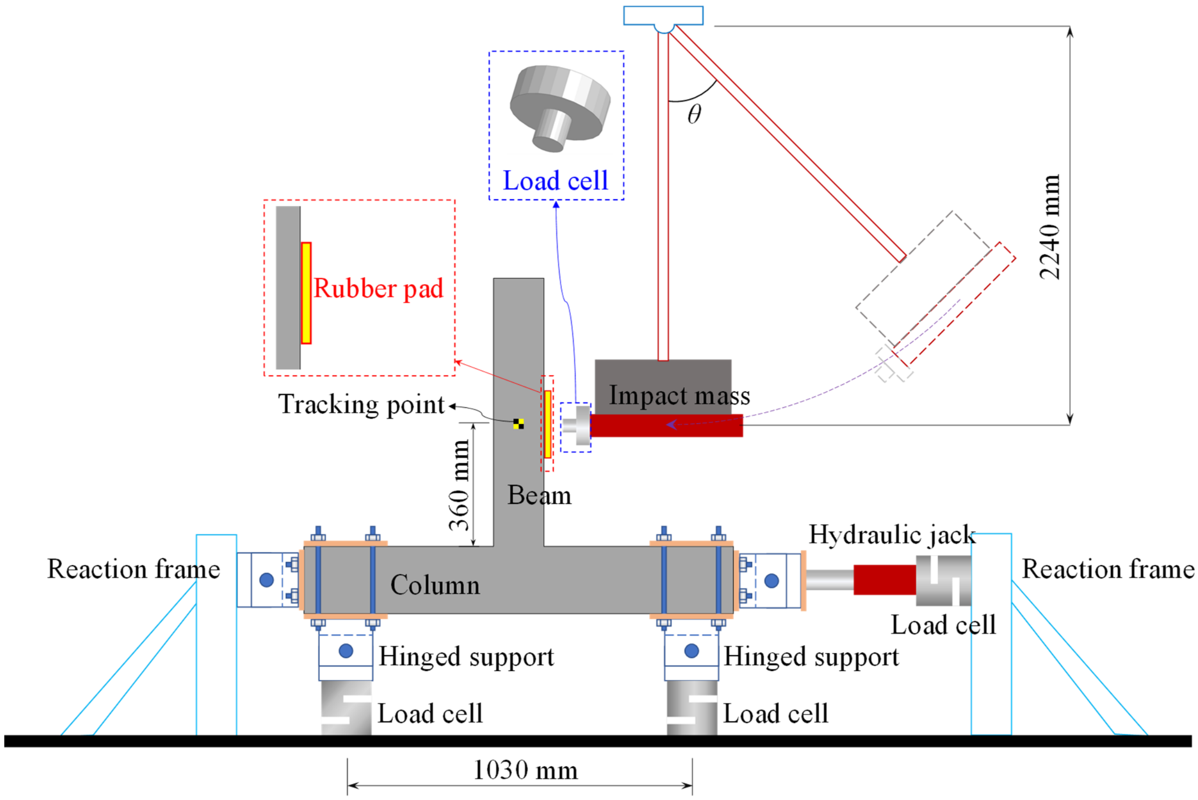

Fig. 3. Pendulum impact test setup with rubber pad.

To simulate the soft contact condition, a natural rubber pad with a thickness of 18 mm was attached at the impact location as shown in Fig. 2 and Fig. 4. The width and length of the rubber pad were 100 mm and 200 mm, respectively. The hardness of the rubber pad was denoted by Shore *A* (the scale of hardness) of 70, provided by the supplier (i.e., Clark Rubber, Australia). The existence of rubber pad at the impact location led to a softer contact condition than the direct impact on specimen. The mass of the rubber pad was 0.41 kg (about 0.07% of the impact mass of 550 kg) in this study, which resulted in negligible inertia effect during impact. Therefore, the existence of rubber pad would have a negligible effect on the measurement of impact force [29, 30]. It is worth mentioning that the rubber pad at the impact location was replaced after each impact to ensure consistent contact stiffness for all the impacts. In addition, the monolithic RC joint MCJ and the PC joint PCJ that were impacted without a rubber pad (direct impact) were reported by the authors in the previous study [27]. The reported results are employed herein to compare the effect of different contact conditions on the impact behavior of beam-column joints. The dimension, reinforcement layout, and material strength of specimens MCJ and PCJ were identical to those of their corresponding specimens MCJ-RP and PCJ-RP (with rubber pad) in this study.

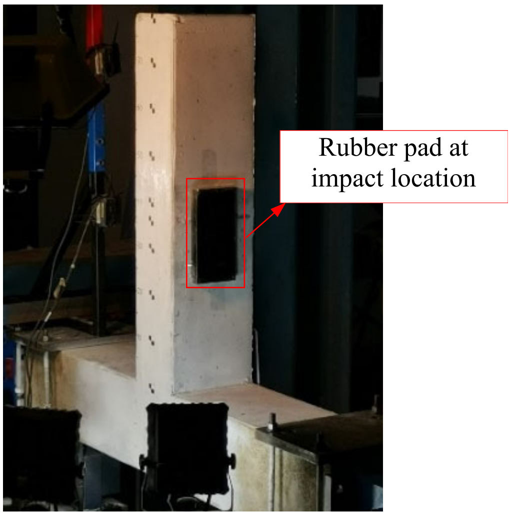

Fig. 4. Rubber pad at impact location.

Table 1 summarizes the release angel (θ) of impactor and impact velocity for each impact. It was found that the actual measured impact velocity was slightly lower than the designed impact velocity due to the slight energy loss of the pendulum system.

Table 1. Summary of impact conditions.

Joint	Impact No.	Release angle (°)	Designed impact velocity (m/s)	Measured impact velocity (m/s)
MCJ-RB	1	30	2.42	2.26
	2	40	3.21	3.06
	3	40	3.21	3.10
	4	40	3.21	3.06
MCJ [27]	1	30	2.42	2.33
	2	40	3.21	3.11
	3	40	3.21	3.19
	4	40	3.21	3.15
PCJ-RB	1	30	2.42	2.23
	2	40	3.21	3.12
	3	40	3.21	3.16
	4	40	3.21	3.09
PCJ [27]	1	30	2.42	2.28
	2	40	3.21	3.16
	3	40	3.21	3.03
	4	40	3.21	3.06

3. Experimental results and discussion

The test results (impulse, reaction force acting on both column ends, and displacement) of beam-column joints with and without rubber pads are summarized in Table 2. It is noted that the dynamic responses of the monolithic RC joint MCJ and PC joint PCJ impacted directly by an impactor as reported in Ref. [27] were adopted herein to compare with those of the specimens with rubber pads MCJ-RP and PCJ-RP obtained in this study to examine the influence of contact conditions on the impact behavior of beam-column joint.

Table 2. Summary of test results.

Joint	Impact No.	Impulse (kN·ms)	Left peak reaction force (kN)	Right peak reaction force (kN)	Maximum displacement (mm)	Residual displacement (mm)
MCJ-RP	1	1907.64	44.56	-51.03	12.12	1.72
	2	2331.45	46.65	-61.44	17.18	3.49
	3	2367.55	50.48	-57.58	17.80	3.50
	4	2354.85	41.84	-51.68	22.87	7.04
MCJ [27]	1	1683.48	63.80	-44.35	13.41	2.87
	2	2244.50	66.25	-50.30	23.21	8.14
	3	2362.42	76.21	-37.32	30.56	16.15
	4	2314.75	65.93	-31.77	37.02	19.49
PCJ-RP	1	1996.45	34.45	-47.03	12.35	1.63
	2	2431.21	46.87	-52.43	23.89	8.63
	3	2540.53	39.04	-44.89	25.61	11.60
	4	2494.59	41.27	-41.61	31.35	15.62
PCJ [27]	1	/	73.66	-46.44	14.05	2.63

2	2244.57	76.01	-54.14	25.42	8.65
3	2392.51	71.99	-36.90	35.74	19.47
4	2246.26	57.76	-27.65	40.30	20.10

Note: "/": not calculated due to the missed impact force in data acquisition system.

3.1. Damage mode

Fig. 5 illustrates the damage mode of beam-column joints with different contact conditions after each impact. The impact loading acted on the right side of beam as presented in Fig. 3. The existence of a rubber pad resulted in a softer contact between impactor and specimens, and thus lower contact stiffness.

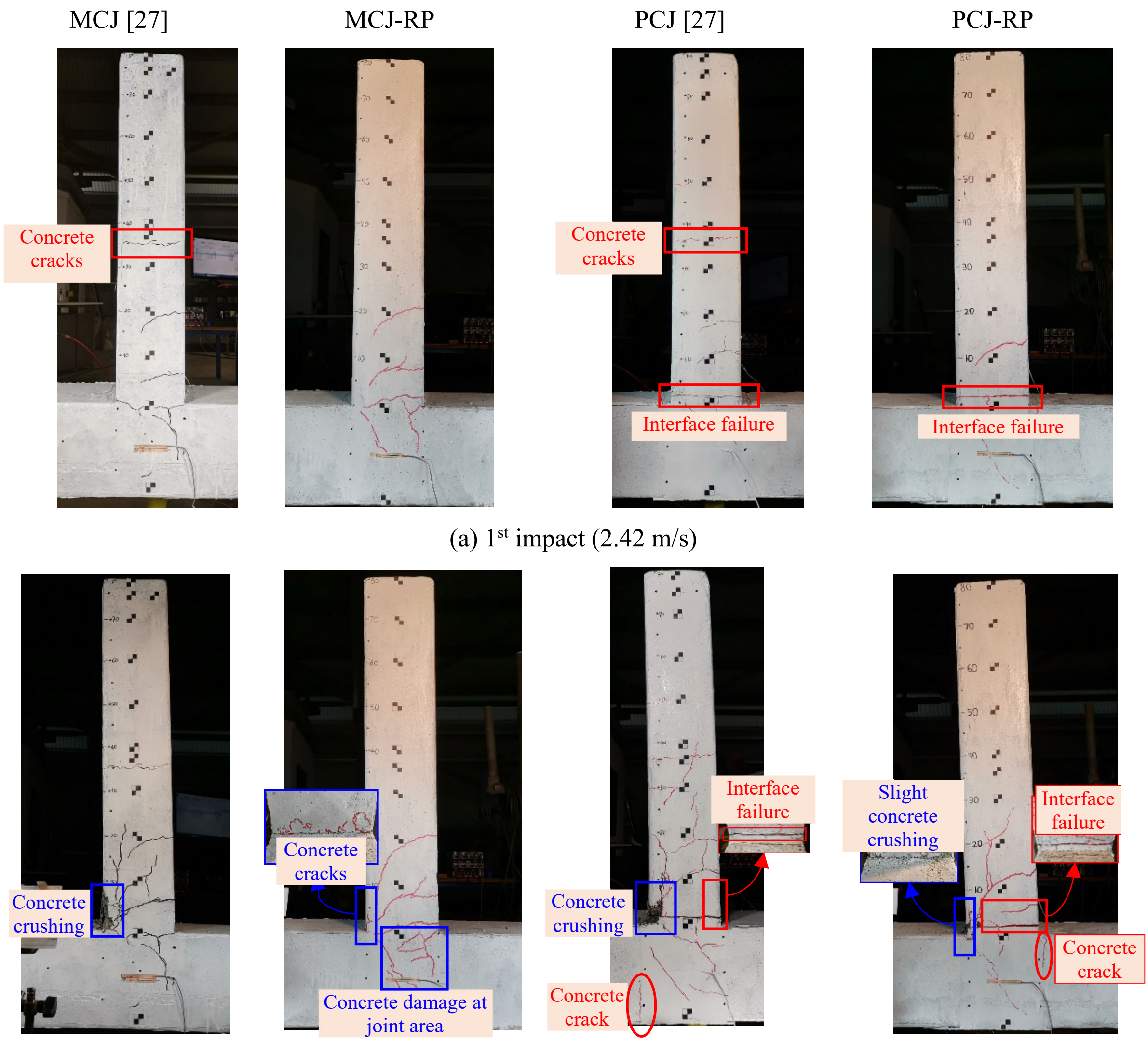

(a) 1st impact (2.42 m/s)

(b) 2nd impact (3.21 m/s)

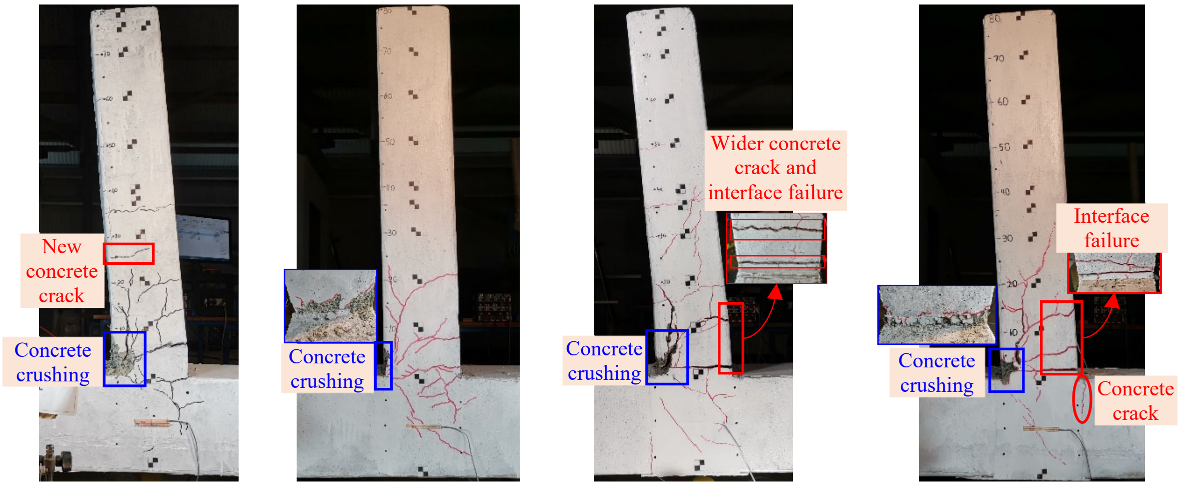

(c) 3rd impact (3.21 m/s)

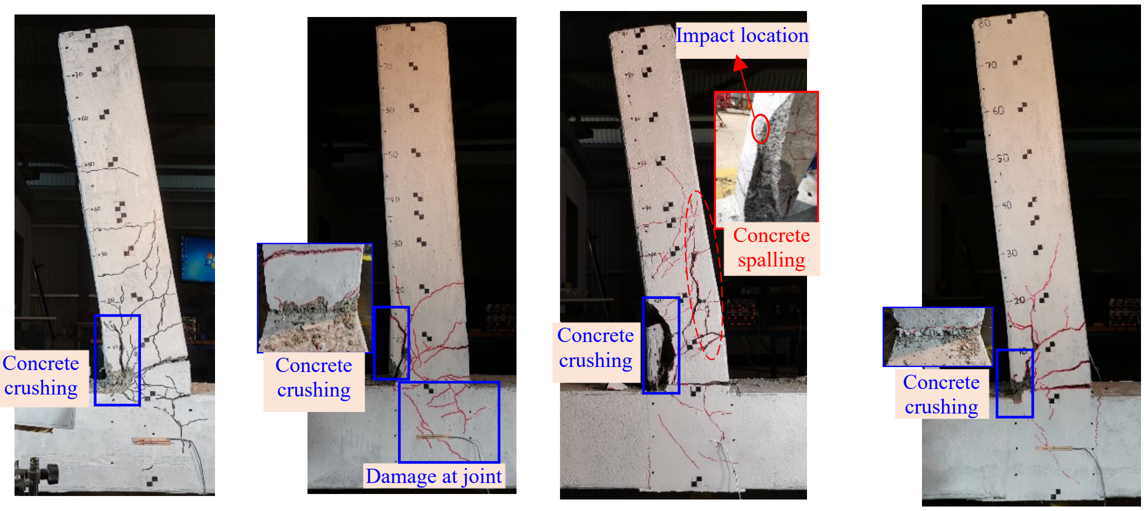

(d) 4th impact (3.21 m/s)

Fig. 5. Damage modes of the four joint specimens after impact.

Fig. 5(a) shows the damage mode of the joint specimens after the first impact. By placing rubber pad at the contact zone, no concrete crack appeared on the beams at the impact location of Specimens MCJ-RP and PCJ-RP. However, concrete cracks at the impact location on the beams were observed on Specimens MCJ and PCJ. This is because the rubber pad reduced the peak impact force and impact loading rate and thus decreased the intensity of stress wave at the impact location. Moreover, tensile concrete cracks appeared on the tension side of beam in all the specimens because of the positive bending moment at this area induced by the impact force. However, only one concrete crack appeared on the right side of PC beam of Specimen PCJ-RP while there were two concrete cracks at these areas in other specimens, which is due to the less connection integrity of PC joint and the reduced impact loading rate by the rubber pad.

The damage modes of beam-column joints after the second impact are shown in Fig. 5(b). Specimens MCJ and PCJ (without rubber pad) experienced severe concrete crushing at the left bottom corner of beam as labeled in the blue rectangle. However, only slight concrete crushing and concrete cracks were observed at the compression area of Specimens MCJ-RP and PCJ-RP. The concrete cracks on the beam generated in the previous impact became wider. Besides, the vertical crack along the left column-to-joint interface appeared in Specimen PCJ while a vertical crack occurred at the upper corner of the right column-to-joint interface in Specimen PCJ-RP, which was due to the difference in left and right reaction forces as illustrated in Section 3.3.

In terms of the damage mode of specimens after the third impact as shown in Fig. 5(c), the specimens without rubber pad (i.e., Specimens MCJ and PCJ) experienced concrete crushing with a larger area than Specimens MCJ-RP and PCJ-RP. More inclined shear cracks on the beam were observed for the specimens without a rubber pad. After the fourth impact as shown in Fig. 5(d), more severe concrete crushing damage occurred at the compressive side of beam and more inclined shear cracks were observed on the beam of the specimens without rubber pad. The presence of rubber pad at the impact location mitigated the damage level on the beam. It can be inferred that the softer impact by using a rubber pad was prone to induce a flexural-governed damage mode while the direct impact resulted in a shear-governed damage mode. In addition, Specimen MCJ-RP experienced more severe damage at the joint zone than Specimen PCJ-RP, owing to the higher connection integrity of the monolithic joint. Upon impact, the specimen dissipated impact energy in the forms of damage of the beam and joint, as well as the deflection of beam. Specimen MCJ-RP with higher connection integrity between beam and joint presented a less deflection, thus more energy dissipation was contributed by the damage of beam and joint. On the other hand, Specimen PCJ-RP presented severe damage along the interface between the beam and joint area, resulting in a larger deflection of beam and therefore less damage to the joint because relatively more impact energy was dissipated by the deflection of beam.

3.2. Impact force

Fig. 6 shows the impact forces of the beam-column joints with or without rubber pads. It should be noted that all the raw impact forces measured by the load cell were filtered using the Butterworth low-pass filter with a cut-off frequency of 1.5 kHz. Specimens MCJ and PCJ showed the impact force profile with an impact force peak followed by a force plateau while Specimens MCJ-RP and PCJ-RP experienced the impact force profile without the primary peak. The impact loading rates for the specimens with rubber pad (i.e., Specimens MCJ-RP and PCJ-RP) were significantly lower than those of the specimens without rubber pad (i.e., Specimens MCJ and PCJ). The average force plateau of Specimen MCJ-RP under four impacts was 62.55 kN, 71.29 kN, 69.88 kN, and 64.91 kN, respectively, which were comparable to 62.46 kN, 71.40 kN, 67.98 kN, and 60.43 kN of Specimen PCJ-RP. Besides, there were significant local peaks in the impact force profiles of Specimen MCJ-RP under the second to the fourth impacts as shown in Fig. 6(b). This is because load cell head penetrated the rubber pad during impact as shown in Fig. 7. When the rubber pad was penetrated by the load cell, the head of load cell contacted the concrete beam directly and induced local peak forces as shown in Fig. 6(b). The impulse acting on the specimens under four impacts is summarized in Fig. 8 and Table 2. It is found that the impulse imposing onto the specimens with rubber pad was higher than that of the specimens without rubber pad. For example, the impulses of Specimen MCJ under four impacts were 1683.48 kN·ms, 2244.50 kN·ms, 2362.42 kN·ms, and 2314.75 kN·ms, respectively, which were lower than 1907.64 kN·ms, 2331.45 kN·ms, 2367.55 kN·ms, and 2354.85 kN·ms of Specimen MCJ-RP, indicating the softer contact condition induced a higher impulse in the impact test. This is because the rubber pad provided cushion effect that led to a longer contact duration of impactor and specimen. Therefore, the impact with rubber pad caused a longer duration than that by the direct impact.

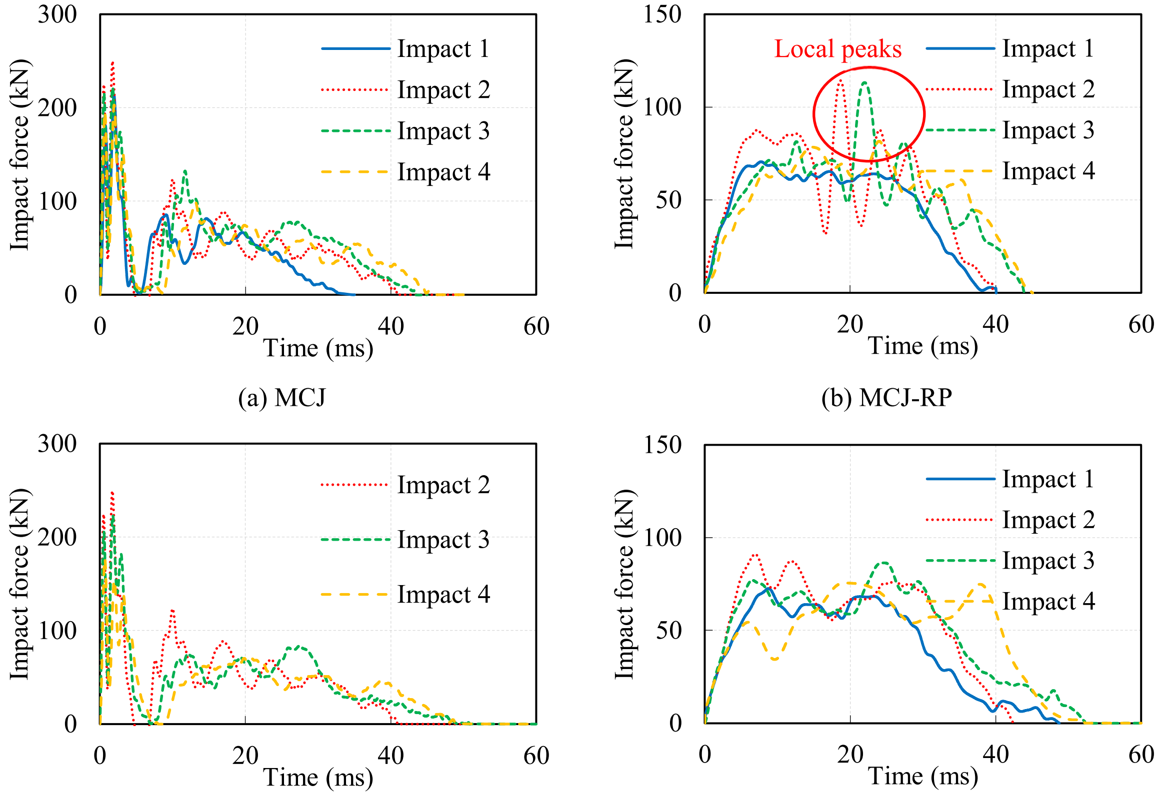

(a) MCJ (b) MCJ-RP

(c) PCJ (d) PCJ-RP

Fig. 6. Time histories of impact force.

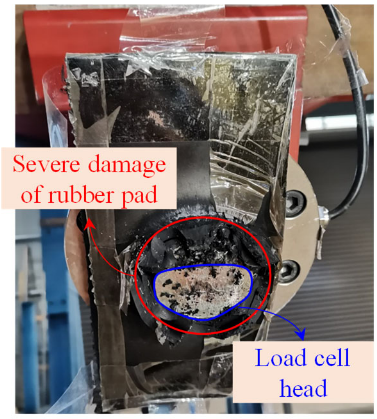

Fig. 7. Severe damage of rubber pad caused by load cell head.

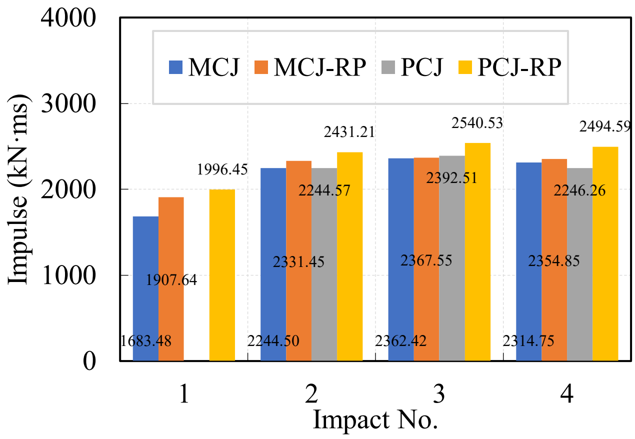

Fig. 8. Impulse acting on specimens.

3.3. Reaction force acting on column

The reaction force acting on the column was recorded by the load cells placed under the specimens as shown in Fig. 3. Since the beam-column joint was constrained by adjacent structure members in reality, it is essential to reveal the reaction force acting on the column under impact loading, which represents the force imposing on the adjacent structural members. Fig. 9 shows the reaction forces acting on the column. The positive reaction force denoted the load cells (under the hinged supports as shown in Fig. 3) was under compression and the reaction force was upward, and vice versa. The legend of reaction force in Fig. 9 ended with "-L" represents the left reaction force and the one ended with "-R" is the right reaction force.

Multi peaks in the left reaction forces were observed, indicating the impact caused the oscillation of the left reaction force. By placing rubber pad at the impact location, the amplitude of oscillation in the left reaction force became smaller due to the reduced peak impact force acting on the joint specimens and the decreased inertia effect along the specimen. Besides, the peak value of right reaction forces in the specimens with rubber pad was slightly larger in general than that of specimens impacted directly. This is because the beam at the tension side and the beam-to-joint interface experienced severer damage by the direct impact, which decreased the joint integrity between the beam and column on the right side. The reduced integrity of joint on the right side led to a decrease in resistance capacity against the external force, indicating smaller reaction force on the right side. In addition, the maximum right reaction force was larger than the left one when the specimens were impacted through a rubber pad, which was opposite to the case of direct impact. For example, under the first impact as shown in Fig. 9(a), the maximum right reaction force of 47.03 kN was larger than the maximum left reaction force of 34.45 kN in Specimen PCJ-RP while the maximum right one of 46.44 kN was smaller than the maximum left one of 73.66 kN in Specimen PCJ. The difference between the left and right reaction forces also explained the different damage at the column-to-joint interfaces as shown in Fig. 5(b), i.e., vertical crack along the left column-to-joint interface as labeled in a red circle in Specimen PCJ and vertical crack at the upper corner of the right column-to-joint interface in Specimen PCJ-RP. It should be noted that the vertical force equilibrium of the specimens during impact event was maintained by the left and right vertical reaction forces as well as the vertical inertia force.

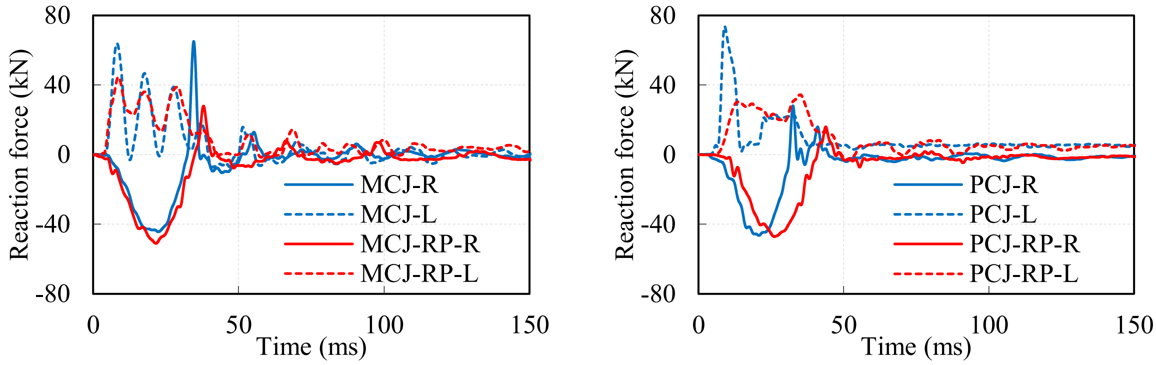

(a) 1st impact

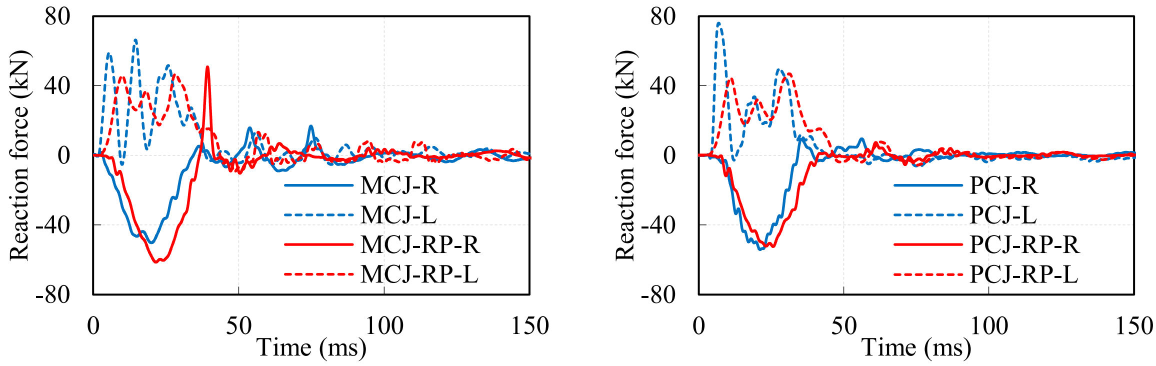

(b) 2nd impact

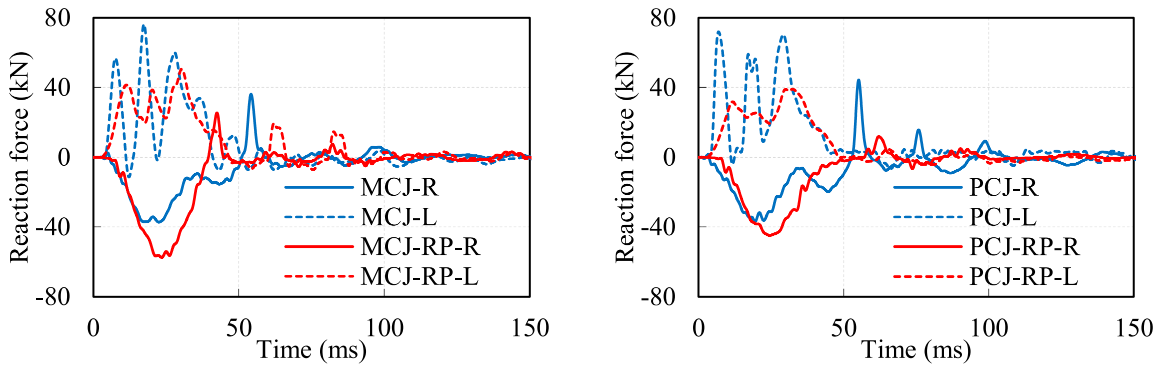

(c) 3rd impact

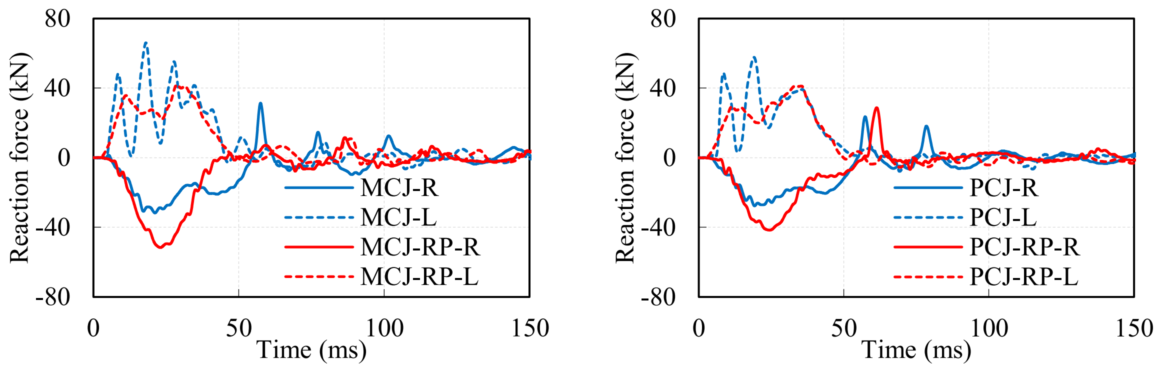

(d) 4th impact

Fig. 9. Time histories of reaction force.

3.4. Displacement at the impact location

Fig. 10 shows the displacement responses of beam-column joints at the impact location. The displacements became larger in each impact as expected due to the increased accumulative impact energy acting on the specimens. It was found that the displacements of specimens with rubber pad were almost zero at the initial stage of the impact because the rubber pad itself experienced crushing at the initial stage of impact. However, the specimens, that were impacted directly, deflected gradually upon impact. This phenomenon meant that the existence of rubber pad delayed the time when the beam began to deform at the impact location.

Fig. 11 compares the maximum and residual displacements of the tested specimens that suffered four impacts. In general, the displacements of specimens with rubber pad were lower than those of specimens impacted directly although the specimens with rubber pads experienced higher impulse as shown in Fig. 8. This is because the rubber pads experienced severe damage and were penetrated by the load cell and thus dissipated a certain amount of impact energy, which led to the decrease of impact energy imparting into the specimens. In addition, the accumulative residual displacements of Specimens MCJ, MCJ-RP, PCJ, and PCJ-RP were 46.65 mm, 15.75 mm, 50.85 mm, and 37.48 mm, respectively after the pendulum impact tests. The softer contact condition with rubber pad mitigated the damage on the specimens and induced a lower accumulative residual displacement. It was found that the accumulative residual displacement of Specimen MCJ was 196% higher than that of Specimen MCJ-RP while the accumulative residual displacement of Specimen PCJ was 36% higher than that of Specimen

PCJ-RP. The influence of using rubber pad on the accumulative residual displacement of the monolithic RC joints was more significant than the PC joints. It is because the PC joints had lower connection integrity between beam and joint area as compared with monolithic RC joints and the wet interface was the vulnerable part in the PC joint, and the damage of interface resulted in larger residual deformation of the structure.

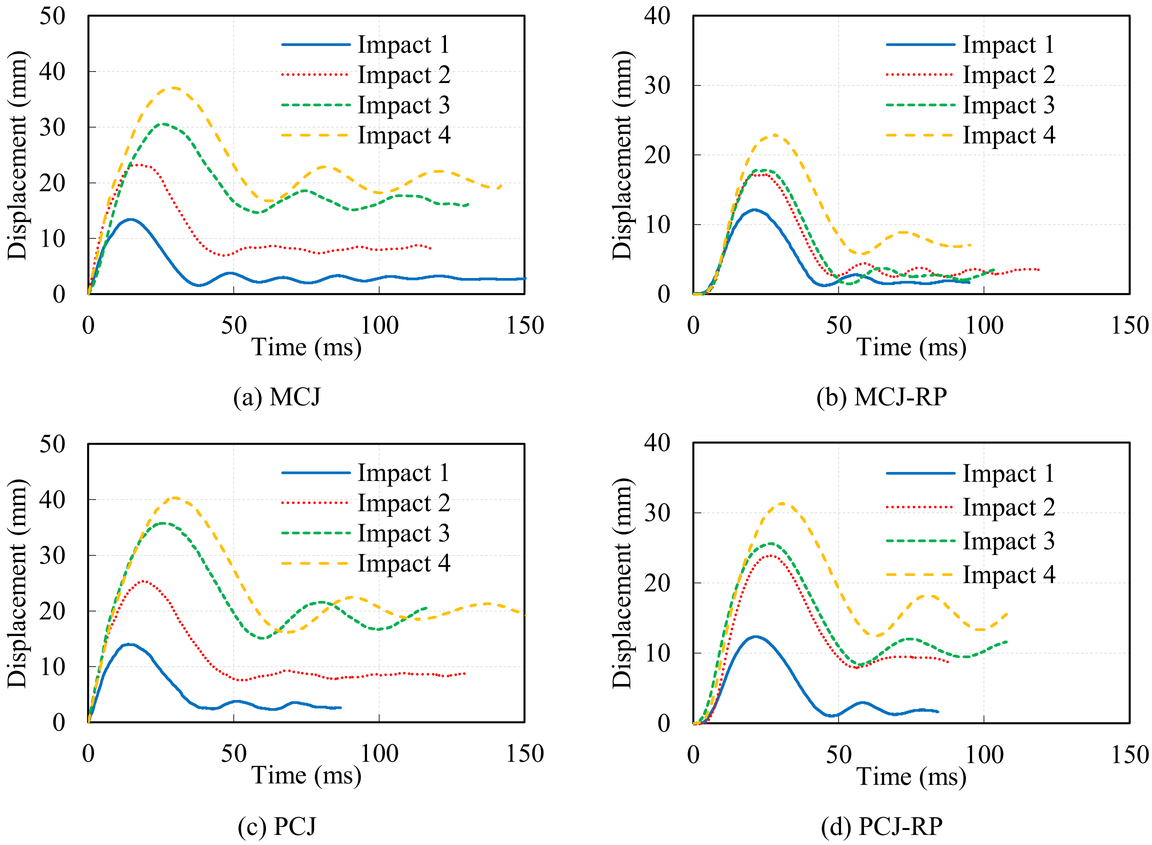

Fig. 10. Time histories of displacement.

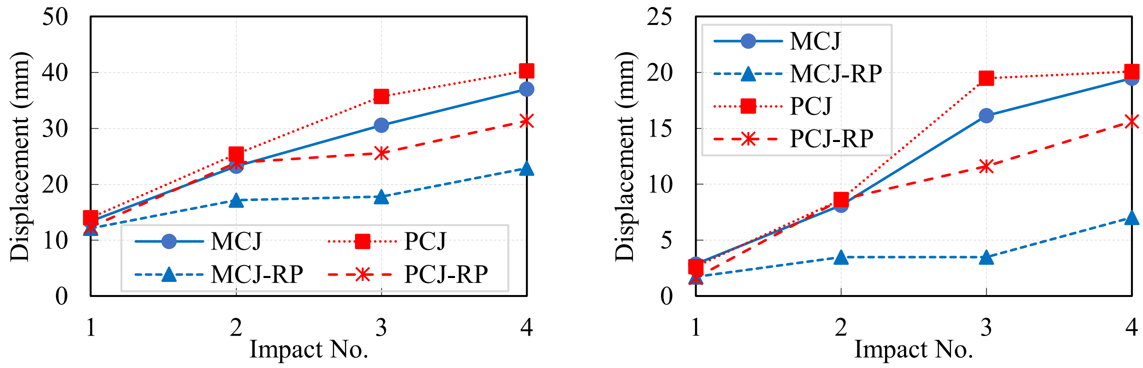

(a) Maximum displacement (b) Residual displacement

Fig. 11. Maximum and residual displacements.

3.5. Discussion of different contact conditions

The experimental results showed that various contact conditions had significant effects on the damage mode, impact force profile, reaction force, and displacement of the beam-column joints under impact loads. Using the rubber pad at the impact location decreased the impact loading rate and the peak impact force, which mitigated the inertia effect and caused less damage on the beam but more severe damage at the joint area. On the other hand, the specimens impacted directly experienced concrete cracking at the impact location of the beam so that more inclined shear cracks and concrete damage were observed on the beam of the specimens. Moreover, the contact conditions also caused different impact force profiles. The softer contact condition by using rubber pad led to the impact force profile with one apparent force plateau, while the impact force profile had a prominent peak impact force followed by a force plateau in the specimens impacted directly. Besides, using the rubber pad reduced the left maximum reaction force but increased the right maximum reaction force due to the decreased inertia effect.

In addition, the rubber pad dissipated a certain amount of impact energy through its deformation and severe damage and thus the energy imparted to the beam became lower, which led to a lower displacement as compared to the displacements of specimens impacted directly. It is worth mentioning that a rigid impactor was employed in the pendulum tests, i.e., the stiffness of the impactor was much higher than that of the specimen. However, the falling object could be broken or damaged during impact in reality, which would dissipate a certain amount of impact energy. This is to say, the damage of either interlayer (such as existing debris) or falling object would reduce the impact energy imparted onto the specimens owing to their damage. To conclude, the rubber pad resulted in a softer contact and reduced the peak impact force and loading rate, which could cause a flexural-governed damage mode of joint specimen. The damage of rubber pad also led to the reduction of impact energy imposing onto the specimens and a lower displacement response. Therefore, various contact conditions should be considered in the design of impact resistance capacity of beam-column joint.

4 Numerical simulation of different impact scenarios

In this section, finite element models of monolithic RC and PC beam-column joints under impact loadings were established using LS-DYNA and verified via the testing data. Based on the calibrated model, the effects of different impact locations and impact loading patterns on the impact behaviors of PC beam-column joints were numerically investigated.

4.1. Calibration of numerical model

4.1.1. Numerical model of joint

Fig. 12 shows the numerical model of the PC beam-column joint. The concrete components, impactor, rubber pad, and steel support plates were simulated by the hexahedral solid elements. The Hughes-Liu beam element was employed for steel rebars. The interfaces between PC and CIPC components were modeled by solid elements. An erosion algorithm based on the maximum principal strain criterion was used to simulate the erosion of concrete elements that experience excessive deformation. The value of the material erosion criterion should be carefully selected and calibrated by trial and error approach. The criterion of the maximum principal strain was determined as 0.005 for the concrete interfaces and 0.1 for the concrete beams and columns in this study. A mesh convergence study was conducted to determine an appropriate mesh size to achieve reliable results with reasonable computational cost. The mesh sizes of the concrete components, rebars, rubber pad, and load cell were determined as 7.5 mm and the mesh size of impactor weight block was set as 50 mm after conducting a mesh convergence study. The steel rebars were coupled with the concrete components by employing the beam-in-solid constrained method. By using this method, the concrete and rebar elements could be meshed separately, which avoided over meshing caused by the concordance between concrete and rebar nodes at joint areas. The eroding surface-to-surface contact was defined for the contact between the load cell and the rubber pad to record the impact force. In addition, the interactions between the column and the steel support plates were defined by the surface-to-surface contact. The steel support plates were hinge-supported to simulate the boundary conditions. The axial force was applied to the column by using the dynamic relaxation method [31, 32] as shown in Fig. 12. The stiffness-based hourglass control method with an hourglass coefficient of 0.05 was adopted to ensure the maximum hourglass energy less than 5% of total energy and the accuracy of numerical results.

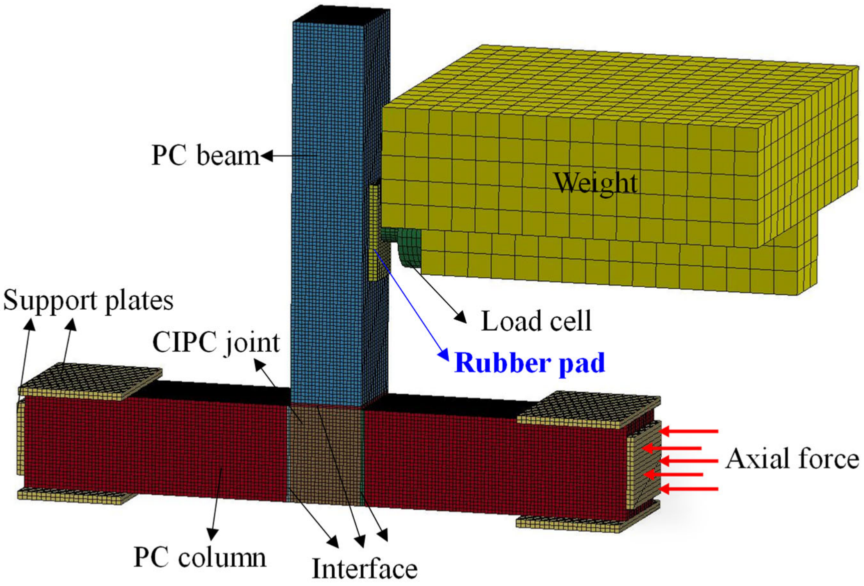

Fig. 12. Numerical model of beam-column joint with rubber pad.

4.1.2. Material models

Concrete components in the numerical models adopted the K&C concrete model (Mat_72R3) which could consider the strain rate effect and concrete damage. This model could be easily defined by inputting the concrete compressive strength and it has been widely employed to predict the dynamic responses of concrete structures under impact and blast loadings [33-35]. The dynamic increase factors (DIFs) of the concrete compressive and tensile strengths [36] were employed in the numerical models to consider the strain rate effect of concrete under impact loading. Moreover, the piecewise elastic-plastic material model (Mat_24) was adopted for the longitudinal rebars and stirrups. The strain rate effect of steel rebar was also considered by defining its DIF model [37]. In addition, the load cell, steel weight block, and steel support plates were simulated by the elastic material model (Mat_01). Besides, the rubber pad at the impact location was modeled by the Mooney-Rivlin rubber model (MAT_27) in LS-DYNA. This rubber material model employed two material constraints (i.e., *A* and *B*) to represent the hyper-elastic behavior of rubber [38-40]. Two material constants (i.e., $A = 0.4825$, $B = 1.9299$) were determined by using the shore hardness (i.e., 70) of rubber pad to characterize the material behavior of rubber after calibrating the numerical models. The detailed material parameters used in the numerical model were tabulated in Table 3.

Table 3. Material parameters used in the numerical model.

Parts	Material model in LS-DYNA	Parameters	Value
Concrete components and interface	CONCRETE_DAMAGE_REL3 (Mat_72R3)	Density	2400 kg/m^3
		Poisson's ratio	0.2
		Compressive strength	64.75 MPa (PC components and interface) 68.34 MPa (CIPC component)
Longitudinal rebar	PIECEWISE_LINEAR_PLASTICITY (Mat_24)	Density	7800 kg/m^3
		Young's modulus	200 GPa
		Poisson's ratio	0.3
		Yield strength	539 MPa
		Ultimate strength	696 MPa
Stirrup	PIECEWISE_LINEAR_PLASTICITY (Mat_24)	Density	7800 kg/m^3
		Young's modulus	200 GPa
		Poisson's ratio	0.3
		Yield strength	523 MPa
		Ultimate strength	692 MPa
Load cell and steel plate	ELASTIC (Mat_01)	Density	7800 kg/m^3
		Young's modulus	200 GPa
		Poisson's ratio	0.3
Rubber pad	MAT_MOONEY-RIVLIN_RUBBER (MAT_27)	*A*	0.4825
		B	1.9299

4.1.3. Comparison of test and numerical results

The numerical models were calibrated against the test results of Specimens MCJ-RP and PCJ-RP under the first impact. The verification of the numerical models of Specimens MCJ and PCJ could be found in Ref. [27]. Fig. 13 compares the damage modes of joints with rubber pads (Specimens MCJ-RP and PCJ-RP) between numerical and test results, which illustrated close agreement between the predicted concrete damage contours and the experimental concrete cracks. The concrete cracks at the tension side of beam were observed in both numerical and test results. In addition, the interface failure in Specimen PCJ-RP was well predicted by numerical simulation.

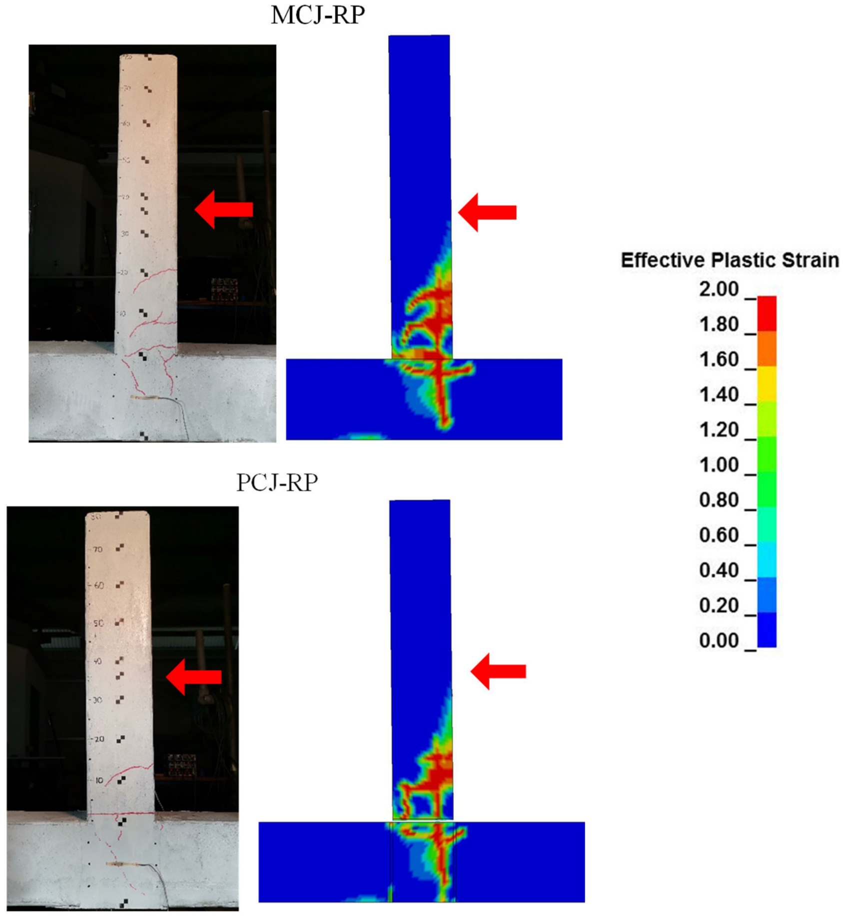

Fig. 13. Comparison of damage mode.

The predicted impact responses were compared with the test results as shown in Fig. 14. Since using rubber pad led to the impact force profile with one apparent force plateau, the average impact force plateau value (F_p) defined in Eq. (1) was employed to quantify the accuracy of numerical simulation [41].

$$F_p = \frac{\int_{t_1}^{t_2} F(t)dt}{t_2 - t_1} \tag{1}$$

where t_1 and t_2 were start time and end time of the impact force plateau as illustrated in Fig.

14(a). The predicted average impact force plateau values in Specimens MCJ-RP and PCJ-RP were 61.62 kN and 62.16 kN, which were comparable to the test results of 62.55 kN and 62.46 kN, respectively. Moreover, as shown in Fig. 14(b), the predicted maximum displacement of 12.12 mm and 12.35 mm for Specimens MCJ-RP and PCJ-RP agreed well with the maximum displacements of 11.43 mm and 10.55 mm as recorded at the tracking point as presented in Fig. 3 in the tests. The predicted residual displacement by numerical model was higher than that from the experimental tests, which might be due to the ideal boundary conditions setting in the numerical models. With the verified numerical models, further numerical studies could be conducted to predict the impact behavior of beam-column joint under different impact scenarios such as different impact locations and impact loading patterns.

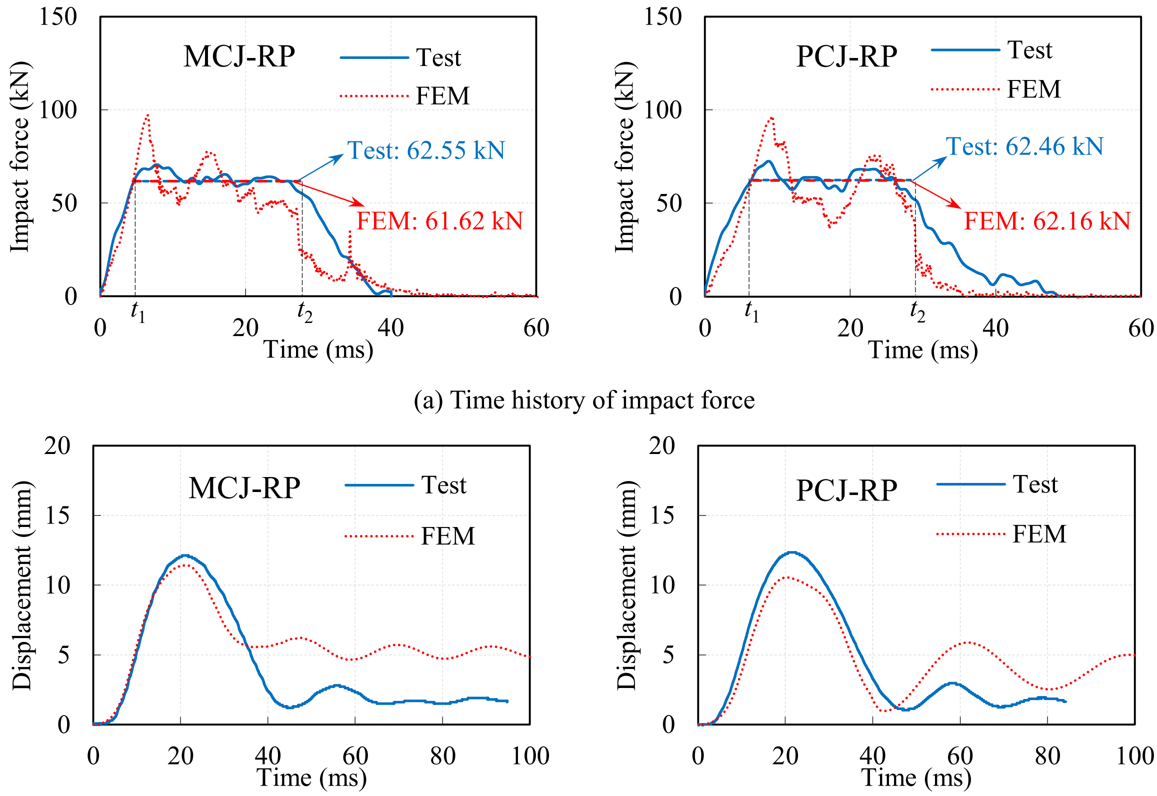

(a) Time history of impact force

(b) Time history of displacement

Fig. 14. Comparison of impact responses of MCJ-RP and PCJ-RP.

4.2. Effect of impact location

Falling objects might impact the lower floor at different locations as shown in Fig. 1(b). Various distances between the impact location and the joint would cause different bending moments and shear forces acting on the joint area and thus mobilize different dynamic responses of beam-column joints. Therefore, the effect of impact location on the impact behavior of PC joint was numerically investigated in this study by using the calibrated numerical model. The impact loads were applied on the PC beam at three locations as shown in Fig. 15, i.e., at the constrained end of beam, at the middle of the beam, and at the free end of beam. The distances between the impact location and the joint area were 100 mm, 360 mm, and 700 mm, respectively. It is noted that the specimens were impacted directly without rubber pad in the following numerical simulations by the identical impact energy (impact mass = 550 kg, impact velocity = 2.42 m/s).

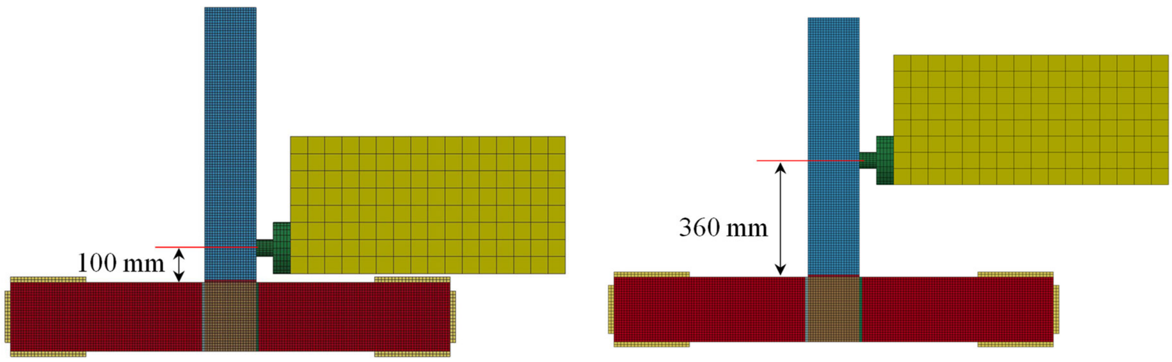

(a) Impact at the constrained end of beam

(b) Impact at the middle of beam

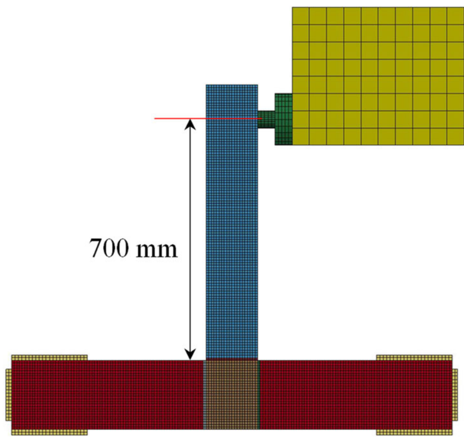

(c) Impact at the free end of beam

Fig. 15. Numerical models of joints subjected to impact loads at different locations.

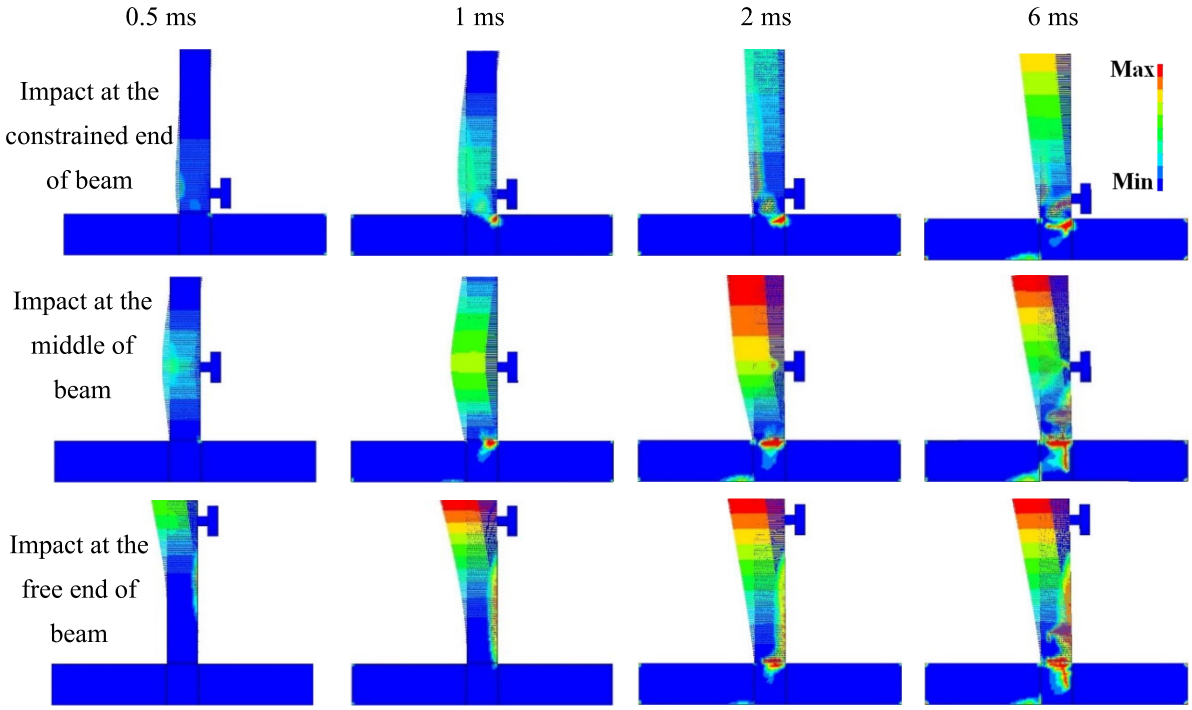

Fig. 16. Lateral deflection contours of joints impacted at different locations.

Fig. 16 shows the lateral deflection contours of joint specimens at different time instants. Under the impacts at three impact locations, the deformation of beam started from the impact points and then extended outwards to the beam ends (free end and the joint area) with the propagation of stress waves and then the beam deflected entirely when the whole beam was mobilized. The increase of the distance between impact point and joint area resulted in the lower global stiffness of beam, which led to the beam presenting global deflection earlier. Fig. 17 shows the damage modes of beam-column joints after impacting at various locations. When the specimen was impacted close to the joint area as illustrated in Fig. 17(a), the damage at the left side of beam appeared first (as shown in Fig. 16 from 0.5 ms to 2 ms) and then the damage at the tension side of beam was observed due to the deflection of beam to the left side as shown in Fig. 16 at 6 ms. For the impact loading acting at the middle of beam as presented in Fig. 17(b), concrete damage at the rear side of the impact location (i.e., at the middle of beam) was observed because of the stress wave reflection and the positive bending moment at this area induced by the impact loading. More shear and flexural concrete cracks occurred on the PC beam as presented in Fig. 17(b). The right side of interface experienced severe damage. When impacted at the free end of beam as shown in Fig. 17(c), more concrete tensile cracks were observed at the right side of beam. It is also interesting to see in Fig. 16 that at 0.5 ms, the response and material damage were limited to the top portion of the beam. This is because, at the initial stage, the response of the entire beam was not activated yet, the damage was caused by the response of the beam in the shortened span and stress wave reflection. As expected, the deflection of beam increased with the increased distance between impact location and joint. The larger beam deflection that caused by a larger bending moment at the connection and led to nearly completed failure at the interface between PC beam and joint as shown in Fig. 17(c). In summary, with the increase of distance between the impact location and the joint, more flexural damage on the beam and more severe damage of wet interface were observed due to the larger bending moment acting on the beam and joint area.

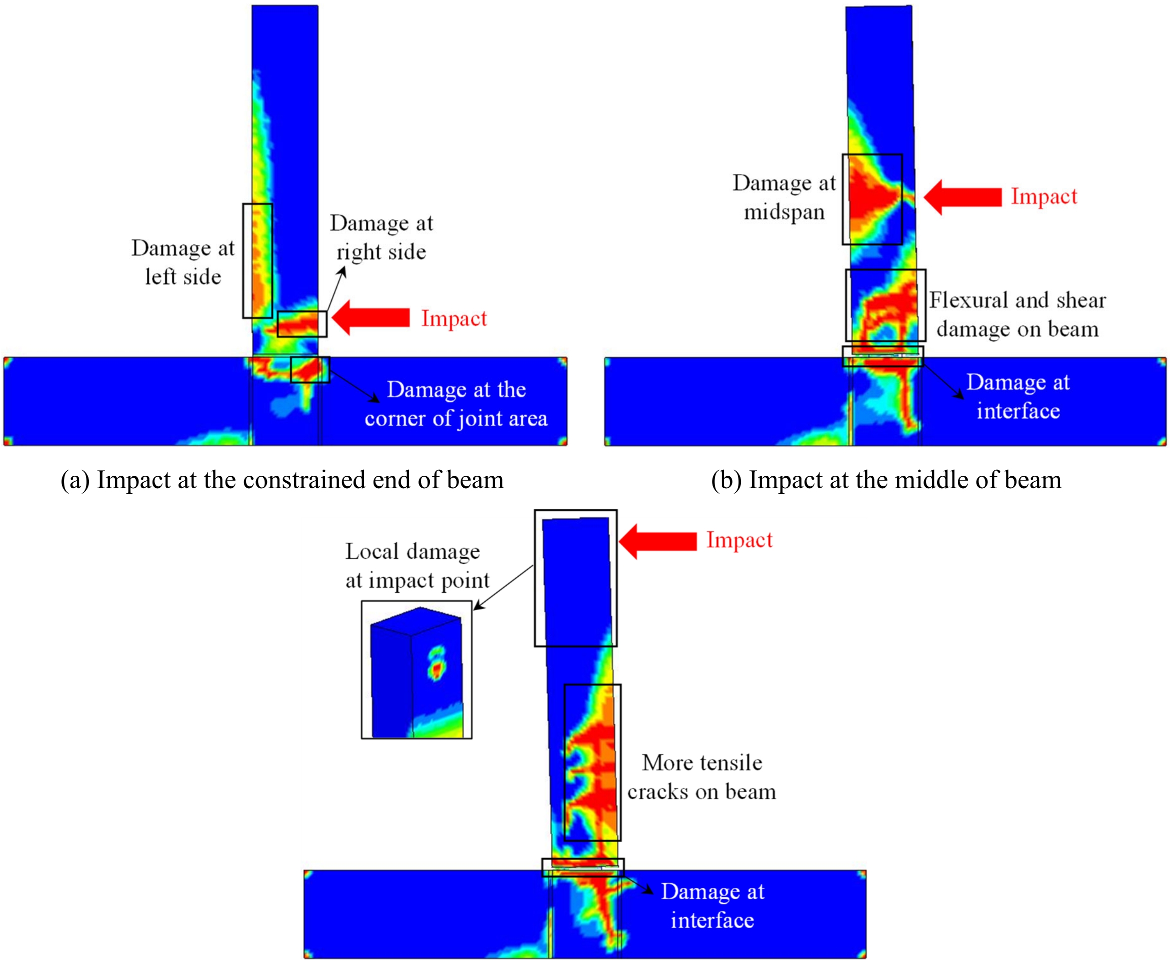

(a) Impact at the constrained end of beam

(b) Impact at the middle of beam

(c) Impact at the free end of beam

Fig. 17. Damage mode of joints impacted at different locations.

Time histories of impact force generated by impacting at different locations are presented in Fig. 18. With the impact distance increased from 100 mm to 700 mm from the beam-column joint, the peak impact force decreased from 335.09 kN to 158.73 kN for the specimens under the same contact condition and identical impact energy. As observed, when the impact force acting on the specimens reached its peak value at the instants of 1.25 ms, 1.0 ms, and 0.63 ms (for the impact distance of 100 mm, 360 mm, and 700 mm from the joint), the beams deflected globally as presented in Fig. 16, which indicates that the global stiffness of beam is activated and the global stiffness affects the peak impact force. This also can be explained by the propagations of stress wave. When the impact location was closer to the joint area, the stress wave propagated from the impact location to the joint area (i.e., boundary surface of the beam) and then reflected back to the impact location within a shorter time. The reflected stress wave resulted in the increment of the impact force [42] and several peaks as shown in Fig. 18.

In addition, the time histories of displacement at the middle of beam are shown in Fig. 19. It is noted that these displacements were measured at the same location, i.e., at the position of the tracking point shown in Fig. 3. As the impact distance changed from 100 mm to 700 mm, the maximum displacement increased from 2.60 mm to 17.17 mm and the residual displacement increased from 0.83 mm to 10.87 mm. This is because the global stiffness of beam with respect to the impact loading was lower when the span length between the joint and impact location was longer. In general, the shorter impact distance between the impact loading point and the joint area presented a higher global stiffness of beam and could induce the shear-governed damage at joint area, higher peak impact force, and less deflection of beam. In contrast, when the impact location was away from the joint area, the specimen presented flexural-governed damage on the beam at the tension side and a larger global displacement response.

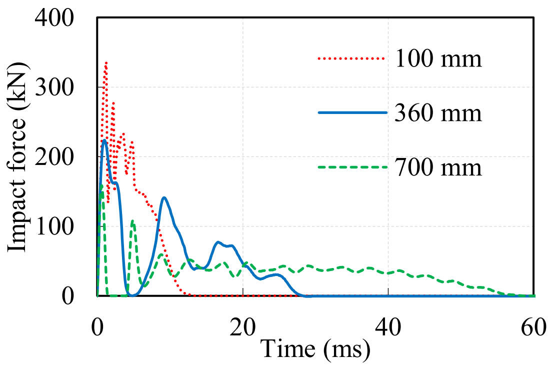

Fig. 18. Time history of impact force of joint impacted at different locations.

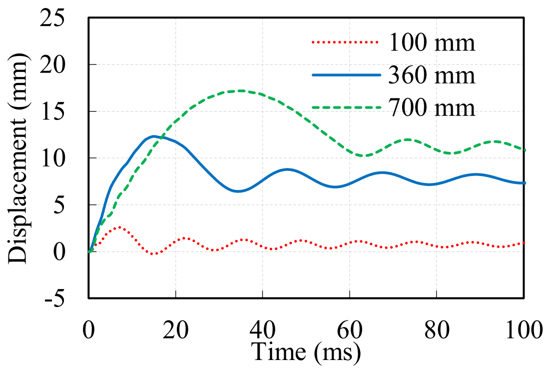

Fig. 19. Time history of displacement of joint impacted at different locations.

4.3. Effect of impact loading pattern

Due to the randomness of falling scenarios, the impact by the falling components might induce a concentrated or a distributed loading as shown in Fig. 1(b) and Fig. 1(c), respectively. The impact force could be generated by an impactor contacting the lower structural components with a smaller area (concentrated pattern) or a larger area (distributed pattern). To understand the effect of various impact loading patterns on the impact behavior of concrete beam-column joints, finite element models of joints were developed as presented in Fig. 20. The concentrated loading pattern was imposed by a cylindrical impactor head with a diameter of 50 mm, which was the same as the impactor in the impact test as shown in Fig. 3. The distributed loading pattern was applied by an impactor with a rectangular contact area of 500 mm × 200 mm as shown in Fig. 20(b). The depth of the impactor was 75 mm. Both specimens were impacted directly by the rigid impactors with identical impact energy (impact mass = 550 kg, impact velocity = 2.42 m/s). It is noted that the center of the distributed loading was assumed at the same location that the concentrated load was applied on the beam, i.e., the distance between the center of the impactor head and the joint area was kept as 360 mm.

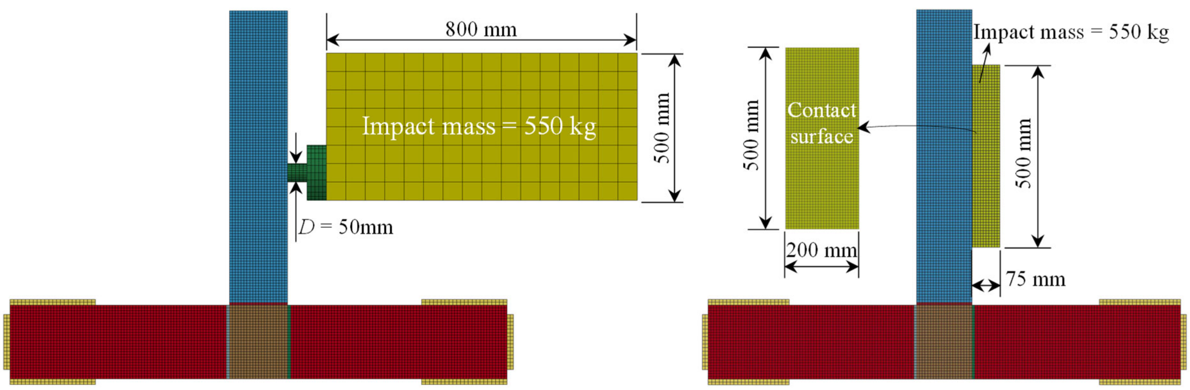

(a) Concentrated impact loading (circular surface with diameter 50 mm)

(b) Distributed impact loading (rectangular surface with area of 500 mm × 200 mm)

Fig. 20. Different impact loading patterns.

PC joints subjected to different impact loading patterns experienced different damage modes as shown in Fig. 21. The concentrated impact loading caused more local concrete damage at the middle of beam, that is, the concrete cracked through the whole depth of beam section as shown in Fig. 21(a). The damage on the left side was caused by stress wave reflection and bending moment at this area induced by the impact loading at the beginning of impact and then extended to the right side of beam section when large global beam response was activated. When the joint was subjected to the distributed impact loading, wider concrete damage was observed on the left side of beam as presented in Fig. 21(b). More severe concrete damage appeared on the tension side of beam because of the large bending moment at this area induced by the distributed impact loading pattern, which generated a larger peak impact force on the beam as presented below. The concrete interface elements experienced total failure as labeled in Fig. 21(b). Besides, severer damage of left PC column-to-joint interface was observed, which indicates that the distributed impact loading caused a larger reaction force acting on the left PC column as mentioned in Section 3.3.

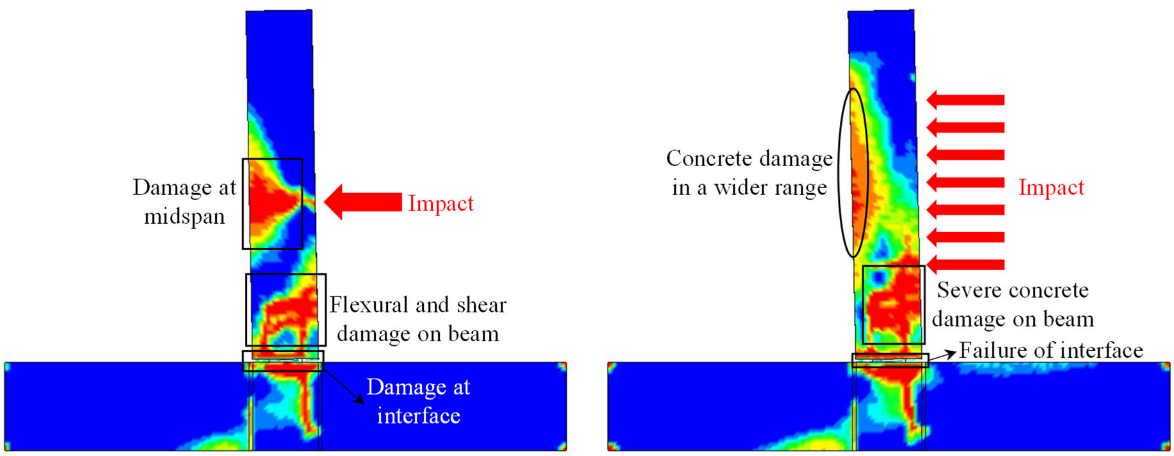

(a) Concentrated impact loading (b) Distributed impact loading

Fig. 21. Damage modes of joints subjected to different impact loading patterns.

Fig. 22 shows the time histories of impact forces imposing on the specimens under different impact loading patterns. It is noted that the concentrated and distributed impact forces were obtained by extracting the contact force between the impactor and the beam from numerical results. When the distributed impact loading was applied on the beam, the peak impact force of 1143.52 kN was much higher than that of 224.06 kN for the specimen subjected to the concentrated impact loading. This is because the distributed impact loading pattern was generated by an impactor with a much larger contact area of 0.1 m^2 at the initial contact than that of 0.002 m^2 for the concentrated impact loading pattern. Under the same impact energy, the larger contact area led to a larger impact force [38, 43]. It is worth noting that the propagation of stress wave in the impactors had limited effect on the peak impact force in this study even for the modeled concentrated loading case. As shown in Fig. 22, the impact force reached the peak at about 1 ms for the concentrated loading case, whereas the dimension of the impactor mass was 800 mm. Taking the wave propagation speed in steel impactor as 5063 m/s, the stress wave would have propagated and reflected a few times inside the impactor mass before reaching the peak impact force, therefore the inertia effect associated to the wave propagation in the impactor was insignificant. Moreover, multiple peaks in the impact force profile of specimen were observed under the distributed impact loading. It is because the beam deformed during the impact event but the flat surface of the rigid impactor block could not always be in full contact with the surface of the beam after the deformation of beam. The impulse applied onto the specimen by distributed impact loading was 1936 kN·ms due to higher peak force and longer impact duration, which was larger than that of 1759 kN·ms under the concentrated impact loading.

In addition, the time histories of displacement at the middle of beam are presented in Fig. 23. The distributed impact loading induced a larger displacement than the concentrated impact loading because the distributed impact loading led to more severe damage in the joint specimen. The maximum and residual displacements were respectively 16.44 mm and 10.32 mm when the beam was subjected to the distributed impact loading, which were larger than the corresponding values of 12.30 mm and 7.59 mm of the specimen subjected to the concentrated impact loading. This is because the distributed impact loading caused more severe damage at the concrete interface as shown in Fig. 21(b), and thus resulted in a larger deflection of the PC beam. In general, the identical impact energy but different impact loading patterns induced very different dynamic responses of beam-column joint. The distributed impact loading resulted in higher impact force, larger displacement response of beam, and more severe damage at joint area, which was deemed as a more dangerous impact scenario to the safety of beam-column joint and thus should be well considered in the design analysis.

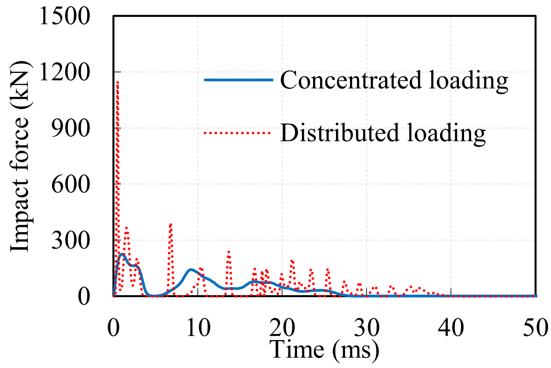

Fig. 22. Time history of impact force.

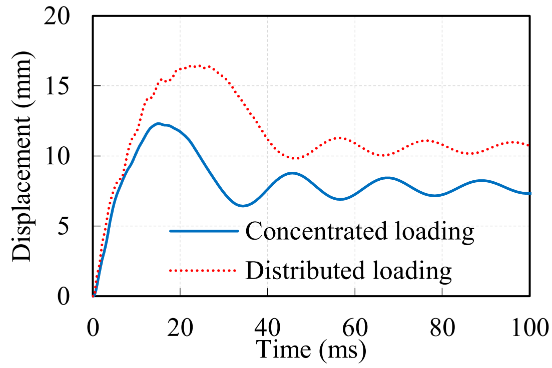

Fig. 23. Time history of displacement at the middle of beam.

5. Conclusions

This study experimentally and numerically investigated the influences of different impact scenarios on the dynamic response of concrete beam-column joints, including contact condition, impact location, and impact loading pattern. Experiments were carried out to study the influence of contact condition on the dynamic response of beam-column joints. Furthermore, finite element models were developed and verified by using the test data. Based on the validated numerical model, the influences of impact location and impact loading pattern on the dynamic response were further investigated. The main findings are summarized as follows.

(1) The direct impact generated a typical impact force profile consisting of a primary impulse followed by a force plateau. Placing a rubber pad between impactor and beam induced a softer contact condition, which led to the reduced impact loading rate and generated an impact force profile without the initial peak impact force but apparent force plateau.

(2) The specimens subjected to direct impact from a rigid impactor experienced more inclined shear cracks on the beam and severer concrete damage at the compression side of the beam and joint area. Placing a rubber pad between impactor and beam generated a softer contact condition and induced more flexural concrete cracks on the beam.

(3) More severe damage at the tension side of the beam and the interface were observed when increasing the distance between the impact location and joint. With the impact location moved from the joint area to the free end of beam, the peak impact force decreased by 53% because of the reduced global stiffness of the beam and interaction of the impactor with the

beam, but the maximum displacement of the beam increased by 560% owing to the larger bending moment at the beam-column joint.

(4) As compared to the concentrated impact loading pattern, the distributed impact loading pattern generated a larger peak impact load and caused much more severe damage at the joint area, wider damaged area at the middle of the beam, and larger displacement response due to the larger contact area between the impactor and the specimen.

In summary, the adverse impact scenarios such as the impact contact condition (i.e., impact directly), impact location (i.e., close to the joint area), and impact loading pattern (i.e., distributed loads), which could occur in reality, were identified and analyzed in this study and should be considered in the impact-resistance design of beam-column joints.

Acknowledgements

The authors acknowledge the financial support from the Australian Research Council (ARC) via Australian Laureate Fellowship (FL180100196). The first author also gratefully acknowledges the financial support from Curtin International Postgraduate Research Scholarship (CIPRS) and Curtin Strategic International Research Scholarship (CSIRS).

References

[1]. Kiakojouri, F., Biagi, V.D., Chiaia, B., and Sheidaii, M.R., *Progressive collapse of framed building structures: Current knowledge and future prospects.* Engineering Structures, 2020. 206: 110061.

[2]. Wang, W.-D., Li, H., and Wang, J.-X., *Progressive Collapse Analysis of Concrete-filled Steel Tubular Column to Steel Beam Connections Using Multi-scale Model.* Structures, 2017. 9: 123-133.

[3]. Joint Aci-Asce Committee 550, *Design guide for connections in precast jointed systems.*

2013: USA.

[4]. Joint Aci-Asce Committee 550, *Guide to emulating cast-in-place detailing for seismic design of precast concrete structures*. 2009: USA.

[5]. International Federation for Structural Concrete, *Seismic design of precast concrete building structures*. 2003, International Federation for Structural Concrete: Lausanne, Switzerland.

[6]. Ding, T., Xiao, J., Zhang, Q., and Akbarnezhad, A., *Experimental and numerical studies on design for deconstruction concrete connections: An overview.* Advances in Structural Engineering, 2018. 21(14): 2198-2214.

[7]. Ghayeb, H.H., Razak, H.A., and Ramli Sulong, N.H., *Performance of dowel beam-to-column connections for precast concrete systems under seismic loads: A review.* Construction and Building Materials, 2020. 237: 117582.

[8]. Eom, T.-S., Park, H.-G., Hwang, H.-J., and Kang, S.-M., *Plastic hinge relocation methods for emulative pc beam-column connections.* Journal of Structural Engineering, 2016. 142(2): 13.

[9]. Im, H.J., Park, H.G., and Eom, T.S., *Cyclic loading test for reinforced-concrete-emulated beam-column connection of precast concrete moment frame.* ACI Structural Journal, 2013. 110(1): 115-125.

[10]. Fan, J.-J., Wu, G., Feng, D.-C., Zeng, Y.-H., and Lu, Y., *Seismic performance of a novel self-sustaining beam-column connection for precast concrete moment-resisting frames.* Engineering Structures, 2020. 222: 111096.

[11]. Ghayeb, H.H., Razak, A.H., and Sulong, R.N.H., *Seismic performance of innovative hybrid precast reinforced concrete beam-to-column connections.* Engineering Structures, 2020. 202: 109886.

[12]. Zhang, Z.-Y., Ding, R., Nie, X., and Fan, J.-S., *Seismic performance of a novel interior precast concrete beam-column joint using ultra-high performance concrete.* Engineering Structures, 2020. 222: 111145.

[13]. Gou, S., Ding, R., Fan, J., Nie, X., and Zhang, J., *Experimental study on seismic performance of precast LSECC/RC composite joints with U-shaped LSECC beam shells.* Engineering Structures, 2019. 189: 618-634.

[14]. Yang, H., Guo, Z., Yin, H., Guan, D., and Yang, S., *Development and testing of precast concrete beam-to-column connections with high-strength hooked bars under cyclic loading.* Advances in Structural Engineering, 2019. 22(14): 3042-3054.

[15]. Kang, S.-B. and Tan, K.H., *Behaviour of precast concrete beam–column sub-assemblages subject to column removal.* Engineering Structures, 2015. 93: 85-96.

[16]. Kang, S., Tan, K., and Yang, E., *Progressive collapse resistance of precast beam–column sub-assemblages with engineered cementitious composites.* Engineering Structures, 2015. 98: 186-200.

[17]. Kang, S. and Tan, K., *Robustness assessment of exterior precast concrete frames under column removal scenarios.* Journal of Structural Engineering, 2016. 142(12): 04016131.

[18]. Kang, S.-B. and Tan, K.H., *Progressive collapse resistance of precast concrete frames with discontinuous reinforcement in the joint.* Journal of Structural Engineering, 2017.

143(9): 04017090.
[19]. Kaewkulchai, G. and Williamson, E., *Modeling the impact of failed members for progressive collapse analysis of frame structures.* Journal of Performance of Constructed Facilities, 2006. 20(4): 375-383.
[20]. Wang, H., Yang, B., Chen, K., and Elchalakani, M., *Parametric analysis and simplified approach for steel-framed subassemblies with reverse channel connection under falling-debris impact.* Engineering Structures, 2020. 225: 111263.
[21]. Li, H., Chen, W., and Hao, H., *Dynamic response of precast concrete beam with wet connection subjected to impact loads.* Engineering Structures, 2019. 191: 247-263.
[22]. Yilmaz, M.C., Mercimek, Ö., Ghoroubi, R., Anil, Ö., and Gültop, T., *Investigation of support type effect on plastic hinges in RC beam under impact load.* Structural Concrete, 2021. 22(4): 2049– 2069.
[23]. Anil, Ö., Yilmaz, M.C., and Barmaki, W., *Experimental and numerical study of RC columns under lateral low-velocity impact load.* Proceedings of the Institution of Civil Engineers-Structures and Buildings, 2020. 173(8): 549-567.
[24]. Gholipour, G., Zhang, C., and Mousavi, A.A., *Numerical analysis of axially loaded RC columns subjected to the combination of impact and blast loads.* Engineering Structures, 2020. 219: 110924.
[25]. Othman, H. and Marzouk, H., *Applicability of damage plasticity constitutive model for ultra-high performance fibre-reinforced concrete under impact loads.* International Journal of Impact Engineering, 2018. 114: 20-31.
[26]. Chen, W., Pham, T.M., Elchalakani, M., Li, H., Hao, H., and Chen, L., *Experimental and Numerical Study of Basalt FRP Strip Strengthened RC Slabs under Impact Loads.* International Journal of Structural Stability and Dynamics, 2020. 20(06): 2040001.
[27]. Li, H., Chen, W., Huang, Z., Hao, H., Ngo, T.T., Pham, T.M., and Yeoh, K.J., *Dynamic response of monolithic and precast concrete joint with wet connections under impact loads.* Engineering Structures, 2022. 250: 113434.
[28]. Ngo, T.T., Pham, T.M., Hao, H., Chen, W., and Elchalakani, M., *Performance of monolithic and dry joints with GFRP bolts reinforced with different fibres and GFRP bars under impact loading.* Engineering Structures, 2021. 240: 112341.
[29]. Li, H., Chen, W., and Hao, H., *Factors influencing impact force profile and measurement accuracy in drop weight impact tests.* International Journal of Impact Engineering, 2020. 145: 103688.
[30]. Hanssen, A.G., Auestad, T., Tryland, T., and Langseth, M., *The kicking machine: A device for impact testing of structural components.* International Journal of Crashworthiness, 2003. 8(4): 385-392.
[31]. Do, T.V., Pham, T.M., and Hao, H., *Stress Wave Propagation and Structural Response of Precast Concrete Segmental Columns under Simulated Blast Loads.* International Journal of Impact Engineering, 2020. 143: 103595.
[32]. Hou, C.-C., Han, L.-H., Liang, Z.-S., and Hu, C.-M., *Performance of concrete-encased CFST subjected to low-velocity impact: shear resistance analysis.* International Journal of Impact Engineering, 2021. 150: 103798.

[33]. Huang, Z., Chen, W., Tran, T.T., Pham, T.M., Hao, H., Chen, Z., and Elchalakani, M., *Experimental and numerical study on concrete beams reinforced with Basalt FRP bars under static and impact loads.* Composite Structures, 2021. 263: 113648.
[34]. Zhang, C., Abedini, M., and Mehrmashhadi, J., *Development of pressure-impulse models and residual capacity assessment of RC columns using high fidelity Arbitrary Lagrangian-Eulerian simulation.* Engineering Structures, 2020. 224: 111219.
[35]. Wu, M., Jin, L., and Du, X., *Dynamic responses and reliability analysis of bridge double-column under vehicle collision.* Engineering Structures, 2020. 221: 111035.
[36]. Hao, Y. and Hao, H., *Influence of the concrete DIF model on the numerical predictions of RC wall responses to blast loadings.* Engineering Structures, 2014. 73: 24-38.
[37]. Malvar, L.J., *Review of static and dynamic properties of steel reinforcing bars.* Materials Journal, 1998. 95(5): 609-616.
[38]. Li, H., Chen, W., and Hao, H., *Influence of drop weight geometry and interlayer on impact behavior of RC beams.* International Journal of Impact Engineering, 2019. 131: 222-237.
[39]. Hallquist, J.O., *LS-DYNA theory manual.* Livermore software Technology corporation, 2006: 531.
[40]. Lee, K., *Effects on the various rubber fenders of a tripod offshore wind turbine substructure collision strength due to boat.* Ocean Engineering, 2013. 72: 188-194.
[41]. Li, H., Chen, W., Pham, T.M., and Hao, H., *Analytical and numerical studies on impact force profile of RC beam under drop weight impact.* International Journal of Impact Engineering, 2021. 147: 103743.
[42]. Pham, T.M. and Hao, H., *Influence of global stiffness and equivalent model on prediction of impact response of RC beams.* International Journal of Impact Engineering, 2018. 113: 88-97.
[43]. Hao, H., Tran, T.T., Li, H., Pham, T.M., and Chen, W., *On the accuracy, reliability and controllability of impact tests of RC beams.* International Journal of Impact Engineering, 2021. 157: 103979.